Available online at www.sciencedirect.com

SCIENCE @ DIRECT®

Journal of Magnetic Resonance 172 (2005) 179–190

JMR
Journal of
Magnetic Resonance

www.elsevier.com/locate/jmr

Spatially encoded NMR and the acquisition of 2D magnetic resonance images within a single scan

Yoav Shrot, Lucio Frydman*

Department of Chemical Physics, Weizmann Institute of Science, 76100 Rehovot, Israel

Received 5 April 2004; revised 31 August 2004
Available online 2 December 2004

Abstract

An approach that enables the acquisition of multidimensional NMR spectra within a single scan has been recently proposed and demonstrated. The present paper explores the applicability of such ultrafast acquisition schemes toward the collection of two-dimensional magnetic resonance imaging (2D MRI) data. It is shown that ideas enabling the application of these spatially encoded schemes within a spectroscopic setting, can be extended in a straightforward manner to pure imaging. Furthermore, the reliance of the original scheme on a spatial encoding and subsequent decoding of the evolution frequencies endows imaging applications with a greater simplicity and flexibility than their spectroscopic counterparts. The new methodology also offers the possibility of implementing the single-scan acquisition of 2D MRI images using sinusoidal gradients, without having to resort to subsequent interpolation procedures or non-linear sampling of the data. Theoretical derivations on the operational principles and imaging characteristics of a number of sequences based on these ideas are derived, and experimentally validated with a series of 2D MRI results collected on a variety of model phantom samples.

Keywords: Ultrafast MRI acquisitions; Spatial encoding; Chirped excitation; Echo-planar imaging

1. Introduction

Two-dimensional (2D) spectroscopy plays a central role in all contemporary applications of nuclear magnetic resonance (NMR) [1]. Although originally proposed and established as a tool for carrying out analytical characterizations on chemical and biochemical samples [2,3] 2D NMR probably finds its widest applicability, in terms of overall measurements carried out, within the context of magnetic resonance imaging (MRI). In spite of the dissimilar information being sought in 2D NMR and 2D MRI experiments, the basic commonalties underlying these two methodologies are well known [4,5]: in both cases pulse sequences are implemented so as to correlate via a 2D Fourier transform, pairs of initial and final (Ω_1, Ω_2) evolution frequencies experienced by the spins. The difference between the two realms lies mainly in the physical nature of the interactions defining these two frequencies: whereas in analytical applications these are given by intrinsic shielding, quadrupolar or spin–spin couplings defined by local molecular environments, MRI strives to suppress this internal information and replace it by artificial frequency shifts dictated by externally applied magnetic field gradients. Though sharing a common ancestry in 2D Fourier Zeugmatography [6], the internal vis-à-vis external character of the interactions being correlated in 2D NMR and MRI have endowed these fields with divergent evolutionary histories. Over the decades 2D NMR remained remarkably close to the paradigm put forward by Jeener, Ernst et al. [7], whereby the Ω_1-induced evolution is indirectly monitored through a step-wise incrementation of an associated time parameter t_1 while Ω_2 is encoded by

---

* Corresponding author. Fax: +972 8 9344123.
E-mail address: lucio.frydman@weizmann.ac.il (L. Frydman).

1090-7807/$ - see front matter © 2004 Elsevier Inc. All rights reserved.
doi:10.1016/j.jmr.2004.09.024

the usual physical acquisition time (t_2). By contrast the gradient-driven nature of the interactions correlated in 2D MRI coupled to the concepts of k-space and of its non-Cartesian sampling using arbitrary gradient waveforms [4,8–10], endowed this branch of the spectroscopy with a much higher data acquisition flexibility. This flexibility arguably finds its ultimate expression in echo-planar imaging (EPI) [11,12], which together with its daughter techniques can provide multidimensional MRI images within a fraction of a second by successively switching on and off the various magnetic field gradients involved in their correlations. A number of alternatives have also been proposed to ease the acquisition or processing requirements demanded by the original EPI scheme [13–15]. Still in all cases, these improvements were based on the pioneering k-space ideas introduced by Mansfield et al.

Over the years a number of attempts were made to extend the time-savings that these “walk through k-space” concepts granted to 2D MRI, toward accelerating the acquisition of other kinds of 2D NMR experiments. Only in those rare instances when the interactions to be correlated could be manipulated with nearly complete efficiency, did such efforts find applicability within purely spectroscopic contexts [16–18]. Very recently, however, we demonstrated an alternative route to the single-scan acquisition of 2D NMR spectra, whose principles are actually different from those of EPI: these new ultrafast schemes replace the usual parametric t_1 encoding of the Ω_1 frequencies to be monitored, by an equivalent spatial encoding of the interactions [19,20]. This is a procedure that unlike the serial incrementation of t_1 values can be parallelized, and thus completed within a single transient. Since the nature of the interactions being correlated or of the transfer processes taking place during the mixing portion of the sequence are not relevant to this parallelization of 2D NMR, it appears that this methodology should be of a general nature. We have described in previous publications comprehensive examples where this is indeed born out in a variety of homo- and hetero-nuclear 2D/3D/4D NMR experiments [19–23]. The present paper turns the focus to MRI and explores the potential provided by these encoding principles toward the ultrafast acquisition of spatially resolved NMR information.

2. Theoretical basis of spatially encoded single-scan 2D MRI

2.1. Spatially encoded single-scan MRI using discrete pulses

As starting point to the present imaging discussion, we illustrate in Fig. 1A one of the schemes we have recently proposed for the single-scan acquisition of multidimensional NMR spectra [19,20]. For the sake of simplicity we have confined it to a single-channel 2D acquisition, where the initial spatial encoding is carried out by a train of frequency-shifted selective excitation pulses applied in synchrony with a square-modulated longitudinal gradient $\partial B_0/\partial z = G_e$. These discrete excitation RF pulses are spaced by constant time intervals Δt_1, differing only by a constant frequency offset $\Delta O = |O_j - O_{j+1}|$. The discrete evolution times t_1 evolved by the spins become then proportional to their $\{z_j\}_{j=1,N_1}$ positions within the sample according to $t_1(z_j) = C \cdot (z_j - z_{N_1})$, where C is a spatio-temporal ratio that for the indicated parameters can be written as $C = G_e \Delta t_1/\Delta O$. This procedure effectively ends up winding a spiral of spin-packets over the sample whose pitch ϕ depends on the internal evolution frequency Ω_1 that acted on the spins: $\phi(z_j) = \Omega_1 t_1(z_j) = C\Omega_1(z_j - z_{N_1})$. When considering a uniform Ω_1 value identical throughout the sample, for instance the chemical shift or J-coupling of a given chemical site, such overall phase encoding amounts to a linear winding of the magnetization. This winding is preserved throughout the mixing

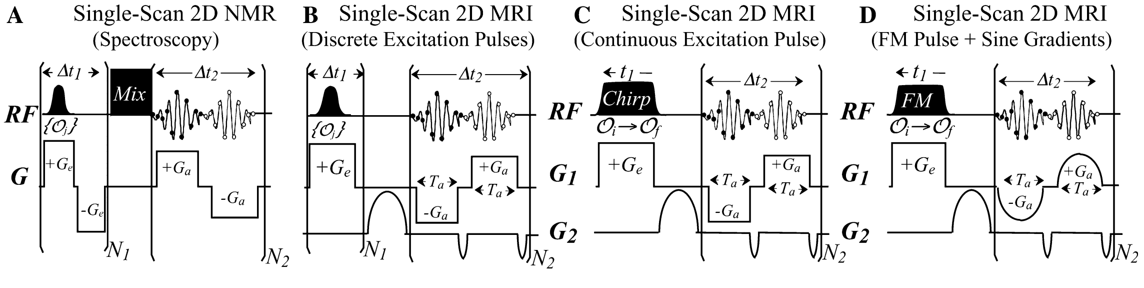

Fig. 1. Comparison between various spatially encoded schemes capable of affording 2D NMR spectra within a single transient. (A) Generic pulse scheme of a 2D NMR spectroscopy experiment based on a discrete uniaxial encoding of the Ω_1 interactions using N_1 excitation pulses, and a subsequent decoding relying on N_2 acquisition cycles. (B) Extension of the pulse scheme in (A) to an imaging setting, where the effective interaction along the indirect domain is given by an unbalanced $G_1 = G_e$ excitation gradient and the direct-domain frequency encoding is imparted in a conventional fashion by a blipped G_2 gradient. (C) Extension of the pulse scheme (B) to the case of a single continuous irradiation pulse. (D) Adaptation of the chirped-pulse scheme in (C) to an acquisition involving oscillatory gradients, which avoids the need for data interpolation thanks to the use of an arccos-type frequency-modulated RF pulse. In all cases wavy lines and dots represent the actual digitization of the signal as a function of (k, t_2); see text for additional details.

period owing to the coherent nature of this process and then, during the course of the acquisition, monitored while in the presence of a longitudinal gradient G_a. Due to its suitable geometric dependence this gradient can unravel the spiraled magnetization and lead to an observable echo, whose position as a function of the acquisition wavenumber $k = \int_0^t G_a(t')\,dt'$ will then be given by $k = -C\Omega_1$. The k-axis thus becomes equivalent to an indirect-domain v_1 frequency axis. Furthermore, such k-driven unwinding process can be undone and redone numerous times by periodically reversing the sign of G_a, allowing one to imprint on this Ω_1-positioned echo an Ω_2 modulation proceeding as a function of t_2.

These principles have been demonstrated experimentally on a variety of spectroscopy experiments where Ω_1 and Ω_2 entailed internal free evolution frequencies, homogeneous for all spins throughout the sample. In an imaging application, however, the frequencies being sought will be given by spatially dependent functions. This in turn prompts the question of how could the principles described in the preceding paragraph be useful for the acquisition of spatial images. There are actually two mechanisms whereby such imaging information might appear encoded. One relates to the line shapes that different sample and gradient profiles may generate when dealing with a sample of non-uniform constitution. This is an effect whose application toward the acquisition of spatially resolved spectral information has been dealt with elsewhere [24]. The second mechanism, the one that constitutes the basis of experiments presented in this work, lies in a separate but important characteristic defining 2D ultrafast NMR acquisitions: the repetitive dephasing/rephasing processes that spins *within individually excited slices* undergo as a consequence of the gradients' actions. Indeed, whereas to a first approximation it is possible to consider the various spin-packets excited by the frequency-shifted train of RF pulses in Fig. 1A as rigid magnetization vectors endowed solely with a position-dependent precession, these spin-packets also possess time-dependent (or more rigorously, k-dependent) amplitudes. Such dependence arises from the dephasing that spins *within* any slice δz undergoing RF excitation will experience under the action of the gradient, and is responsible for the "enveloping" properties discussed elsewhere in connection to the amplitudes of peaks in ultrafast NMR [20,23].

These dephasing effects can provide a new approach toward the acquisition of nD spatially localized MR images in a single scan. To visualize how this comes to happen consider the transformation of the spectroscopy-oriented scheme introduced in Fig. 1A, to the imaging-oriented one presented in Fig. 1B. Two main changes underlie this transformation: one is the incorporation of a net $\Omega_1 = G_e \cdot z$ evolution frequency via the removal of the gradient echo procedure previously employed during the excitation; the other is the incorporation of an orthogonal gradient-driven frequency shift $\Omega_2 = G_2 \cdot r_2$ ($r_2 = x$ or y) for the sake of encoding, in a usual k-incremented fashion, a second spatial dimension during the course of the acquisition. Notice that removing the gradient echo conditions originally employed in the excitation actually simplifies the protocol, as the initial G_e gradient can now be applied in a constant manner throughout the excitation. To analyze the state of the spins at the conclusion of this excitation we shall assume no chemical shift or J-coupling evolutions; given the absence of refocusing gradients during the excitation, the applied train of RF pulses will then generate N_1 sequentially excited spin-packets with average evolution phases

$$\begin{aligned}\langle \phi(z_j)\rangle &= \Omega_1(z_j)\cdot t_1(z_j) = G_e z_j \cdot C(z_j - z_{N_1}) \\ &= \frac{\Delta t_1}{\Delta O} G_e^2 z_j (z_j - z_{N_1}), \quad j = 0,\ldots,N_1 - 1, \qquad (1)\end{aligned}$$

and individual intra-slice dephasings

$$\Delta\phi(z_j) \approx t_1(z_j)\cdot G_e|z_j - z_{j-1}| \approx \frac{\Delta t_1}{\Delta O} G_e^2 (z_j - z_{N_1})\cdot \delta z. \qquad (2)$$

Here we have assumed for simplicity that for every slice its evolution time $t_1(z_j)$ is much larger than the actual RF pulse width,[1] and defined $\delta z = |z_j - z_{j-1}| = \Delta O/G_e$ as the widths of the individually excited slices. An additional assumption worth introducing at this point is that all excitation pulses used had identical shapes $E(t)$, leading in turn to identical intra-slice excitation profiles $P(\delta z)$ proportional to the Fourier conjugate of $E(t)$—*sinc*-type profiles for a train of rectangular pulses, Gaussian profiles when using Gaussian-shaped pulses, etc. The overall magnetization of the sample prior to beginning the acquisition process can then be described as

$$M(k=0) = \sum_{j=0}^{N_1-1} A(z_j) e^{i\langle\phi(z_j)\rangle} \int_{\text{slice}} P(\delta z) e^{i\Delta\phi(z_j)}\, d(\delta z). \qquad (3)$$

The $A(z_j)$ coefficients in this equation describe the contributions arising from the individual spin-packets into which the sample was partitioned by the selective excitation train, and constitute in essence the voxel imaging elements one is trying to obtain. Notice that these coefficients are multiplied by phase factors $e^{i\langle\phi(z_j)\rangle}$ that, possessing a quadratic dependence on the position z_j, will not be refocused by the application of an acquisition gradient. This will prevent the generation of a common high-resolution k-echo throughout the sample, a feature that may be fundamental in high-resolution spectroscopy but not in an imaging context where no homogeneous frequency behavior is expected from the sample as a whole anyhow. By contrast the linear dependence of the slices' dephasing on z_j, embodied by the $e^{i\Delta\phi(z_j)}$

---

[1] Violating such assumption simply shifts the resulting z-image by a constant factor.

phase factor, allows for the sequential imaging of the sample via the application of the longitudinal acquisition gradient G_a that progressively brings into focus spin-packets corresponding to different z slices. Such sequential refocusing and defocusing of the spin-packets can be appreciated from calculating the magnitude of the signals detected during the course of the acquisition, as the sample accrues an extra $k = \int_0^t G_a(t')\,dt'$ phase factor:

$$|S(k)| \propto \left| \sum_{j=0}^{N_1-1} A(z_j) e^{i\langle\phi(z_j)\rangle} e^{ik\cdot z_j} \int_{\text{slice}} P(\delta z) e^{i\frac{\Delta t_1}{\Delta O} G_e^2 (z_j - z_{N_1})\delta z} e^{ik\delta z}\, d(\delta z) \right|. \tag{4}$$

The actual result of the intra-slice integral in this expression will depend on the $P(\delta z)$ profile, and thereby on the pulse shape employed to achieve the spatial encoding. Yet for all normal excitation conditions this integral will peak whenever the phase involved in its exponent fulfills

$$\frac{\Delta t_1}{\Delta O} G_e^2 (z_j - z_{N_1}) + k = 0 \tag{5}$$

at which point the detected signal will take a value proportional to the sample's profile: $|S(k)| \propto |A(z_j)|$. It follows from these arguments that the refocusing gradient successively probes the spins' density $|A(z_k)|$ at positions

$$z_k = z_{N_1} - \frac{\Delta O}{\Delta t_1} \frac{1}{G_e^2} k. \tag{6}$$

This expression allows for a straightforward calculation of the spatial resolution and field-of-view (FOV) characteristics associated to this new image-retrieving protocol: resolution will be limited to the width of the excited slices $\delta z = |\Delta O / G_e|$, while setting k to its maximum absolute value $k_{\max} = |G_a T_a|$ leads to $\mathrm{FOV} = |\Delta O G_a T_a / \Delta t_1 G_e^2|$.

Eq. (6) implies that when applying a train of frequency-shifted excitation pulses and subsequently a constant decoding gradient G_a, the acquisition k axis de facto unveils the conjugate z profile of the spins. Fig. 2 illustrates this unusual procedure whereby a k wavenumber effectively becomes its conjugate z coordinate, with a numerical 1D simulation based on integrating the Bloch equations governing the behavior of a large number of z spin-packets subject to the pulse sequence in Fig. 1B. As can be appreciated the method's faithfulness to the original sample shape is acceptable, even if the resolution is somewhat coarse due to the discrete nature of the excitation. The extension of this new imaging principle to single-scan 2D MRI is further illustrated with experiments below.

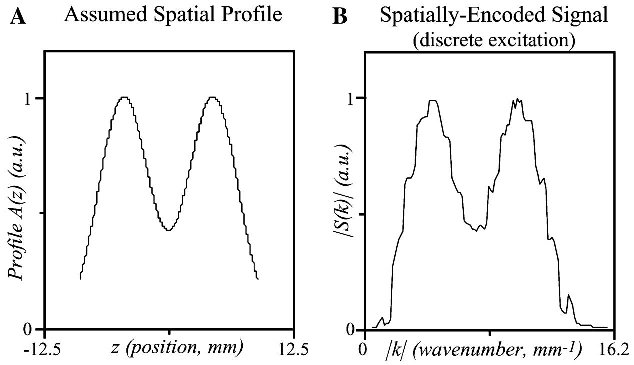

Fig. 2. Capability of the pulse sequence introduced in Fig. 1B to spatially map a profile as a function of the $0 \leqslant k = G_a t \leqslant G_a T_a$ acquisition wavenumber. (A) Assumed $A(z)$ spatial profile for the sample, given by 501 pixels spread over 18 mm. (B) Calculated $|S(k)|$ signal expected upon implementing on a sample with the $A(z)$ profile in (A), the sequence in Fig. 1B with the following parameters: $G_e = 8.1$ kHz/mm, $N_1 = 15$ square excitation pulses, $\Delta O = 10$ kHz, $\Delta t_1 = 0.1$ ms, $G_a = -16.2$ kHz/mm, $T_a = 1$ ms. In an actual 2D MRI experiment this signal would correspond to the first of the $2N_2$ echoes monitored as a function of t_2, which would then subject to an additional G_2 encoding. The image in (B) resulted from numerically co-adding the contributions arising from spin packets placed at different z coordinates throughout the sample, each of them subject to a time-propagation as dictated by their individual time-dependent Bloch differential equations.

2.2. Spatially encoded MRI using chirped pulses

The simple task demanded from the excitation-gradient/RF-pulse combination in the scheme just described—essentially that they succeed in imparting on spin-packets at different z coordinates a sequential dephasing increasing linearly with position—implies that several variants and improvements can be implemented on the basic scheme depicted in Fig. 1B. One of the most evident ones relates to the possibility of reducing the duration of the discrete pulses employed in the excitation scheme until taking them to a very short—essentially δ-like—pulse width limit. As no gradient interruptions or reversals are involved in the excitation protocol of Fig. 1B, assuming such δ-pulse limit eventually leads to replacing the original train of frequency-shifted pulses by a single frequency-swept pulse, a chirp pulse where the offset of the RF is linearly varied from one extreme of the gradient-imposed FOV to the other (Fig. 1C). Key acquisition parameters in this chirp excitation mode will be the nutation frequency Ω_{RF} associated to the RF field, as well as the rate $R = \lim_{\Delta t_1 \to 0} \frac{\Delta O}{\Delta t_1} = \frac{\partial O}{\partial t_1}$ characterizing how rapidly are frequency offsets being swept during the course of the pulse.[2] The well-known adiabaticity parameter $\alpha = |(\Omega_{RF})^2 / R|$ defines then the characteristics of the sweep [25]. Within the context of an efficient excitation this parameter is desired to be in the order of unity, as neither a sudden passage ($\alpha \ll 1$) nor an adiabatic sweep

---

[2] Strictly speaking it is $-R$ that defines the rate of the frequency sweep. This is a consequence of Δt_1 having a sign opposite to the time defining the progress of the chirp pulse: the first z position to be excited by this pulse will be subject to the maximum t_1 evolution time $t_1^{\max}$, whereas the last z position will be characterized by $t_1 = 0$.

($\alpha \gg 1$) can provide for the sequential spatial excitation and ensuing dephasing characteristics demanded by the experiment. It follows that the objective of this chirped excitation pulse is different from the frequency-swept scheme recently discussed within the context of single-scan 2D NMR spectroscopy, where the goal was to implement an adiabatic inversion of the spins [26].

On attempting to describe the imaging methodology that will arise from the action of a single frequency-swept encoding pulse and of a subsequent gradient-driven decoding, it is convenient to partition the analysis into two separate aspects. One involves deriving the phases accumulated by the spins along the various stages of the frequency-swept spatial encoding. A second aspect involves describing the actual nutation effects imparted by the RF field, and their optimization in terms of maximizing the observed signal intensity. We relegate this second aspect of the analysis to an Appendix, and begin with the first of these accounts by disregarding the actual details of the spin nutation altogether. To extend the discrete imaging principles summarized in Eqs. (1)–(6) to the case of a continuous frequency-swept RF pulse we shall assume that, at any given instant t_1, the only consequence of applying a pulse possessing an instantaneous offset $O(t_1)$ is to trigger the excitation of all spins placed at a particular z coordinate fulfilling $O[t_1(z)] = G_e \cdot z$. Two main differences need then be considered upon extending the previous discrete irradiation analysis, to the calculation of the phases accumulated by spins excited under the action of a chirped RF. One concerns the appearance of a new contribution to the overall phase accrued by the spins, which stems from the unavoidable phase incrementation that a continuously frequency-swept RF undergoes over the course of its pulsing. We denote this new additional contribution as ϕ_{pulse}. Taking into account that as the excitation proceeds through the sample ϕ_{pulse} accumulates while the corresponding $t_1(z)$ evolution times become progressively smaller, such additional phase incrementation can be written as

$$\begin{aligned}\phi_{\text{pulse}}(z) &= \int_0^{t_1^{\max}-t_1(z)} O(t')\,\mathrm{d}t' \\ &= \int_0^{t_1^{\max}-t_1(z)} [O_i - R\cdot t']\,\mathrm{d}t' \\ &= \int_0^{t_1^{\max}-t_1(z)} [O_f + R\cdot(t_1^{\max} - t')]\,\mathrm{d}t', \qquad (7)\end{aligned}$$

where $O_i = G_e \cdot z_i$ and $O_f = G_e \cdot z_f$ are the initial and final frequencies of the chirp pulse, assumed to have proceeded at a constant R rate over a time $t_1^{\max} = G_e/R(z_i - z_f)$. The z-dependence of ϕ_{pulse} derives from the fact that the evolution times t_1 characterizing different z coordinates are different: $t_1(z) = G_e/R(z - z_f)$. Replacing this dependence into Eq. (7) leads to

$$\phi_{\text{pulse}}(z) = \frac{G_e^2}{R} z_f(z_i - z) + \frac{G_e^2}{2R}[(z_i - z_f)^2 - (z - z_f)^2]. \qquad (8)$$

A second difference arising in the frequency-chirp scenario stems from the lack of discretely excited slices, and therefore of the $\Delta\phi$ phase dispersion previously associated to a slice of thickness δz (Eq. (2)). What will still hold, however, is that spins at different coordinates z will accumulate different precession phases due to the differing times at which the gradient G_e began acting upon them. This phase follows from a continuous version of Eq. (1), and yields

$$\phi(z) = \Omega_1(z) \cdot t_1(z) = G_e z \cdot C(z - z_f) = \frac{G_e^2}{R} z(z - z_f). \qquad (9)$$

Notice that in comparison with the discrete case the inverse chirp rate R^{-1} takes the place of $\Delta t_1/\Delta O$, and the final z_f position replaces the last discrete coordinate z_{N_1}. The overall signal intensity measurable upon winding spins with the phases in Eqs. (8) and (9), and then unwinding them with the usual $k\cdot z = \lfloor \int_0^t G_a(t')\,\mathrm{d}t \rfloor \cdot z$ acquisition phase, will be

$$\begin{aligned}|S(k)| &\propto \left| \int_{\text{all } z} A(z)\cdot \mathrm{e}^{\mathrm{i}\phi(z)} \cdot \mathrm{e}^{\mathrm{i}\phi_{\text{pulse}}(z)} \cdot \mathrm{e}^{\mathrm{i}kz}\,\mathrm{d}z \right| \\ &= \left| \int_{\text{all } z} A(z) \cdot \mathrm{e}^{\mathrm{i}\Phi(z)}\,\mathrm{d}z \right|. \qquad (10)\end{aligned}$$

By contrast to the previous analysis this chirp-derived signal is not made up of contributions arising from different discrete slices, and therefore it is not possible to claim a k-driven refocusing of the spins on the basis of intra-slice arguments. On the other hand it is clear that the action of the k wavenumber in this situation will not be unlike the one detailed for the discrete excitation scenario: the refocusing gradient G_a will still bring spins at adjacent z coordinates sequentially into focus, driving the constructive interference between their magnetizations and thereby enabling a macroscopic measurement of their associated $A(z)$ profiles. A necessary and sufficient condition for the k wavenumber to create such constructive interference within the neighborhood of a given z coordinate, is that the overall evolution phases of spins at this particular z_k position present a slowly varying spatial dependence. Mathematically, this demands that the phase $\Phi(z)$ fulfill the stationary condition

$$\begin{aligned}\left(\frac{\partial \Phi}{\partial z}\right)_{z=z_k} &= \frac{\partial}{\partial z}\left[\frac{G_e^2}{R} z_f(z_i - z) + \frac{G_e^2}{2R}\left[(z_i - z_f)^2 - (z - z_f)^2\right]\right. \\ &\qquad \left. + \frac{G_e^2}{R} z(z - z_f) + kz\right]_{z=z_k} = 0. \qquad (11)\end{aligned}$$

Simple algebra reveals that for a given k value the spins fulfilling such condition lie at

$$z_k = z_f - \frac{R}{G_e^2} k, \qquad (12)$$

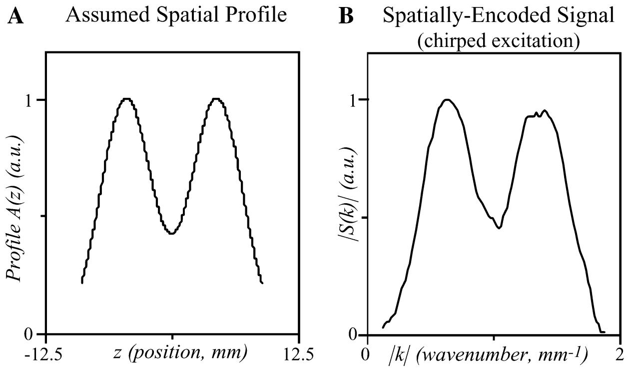

Fig. 3. Idem as in Fig. 2, but this time assuming the application of a frequency-chirped pulse sequence like the one introduced in Fig. 1C. Parameters for such pulse sequence included $G_e = 8.1$ kHz/mm, $t_1^{max} = 0.2$ ms, $O_i = -O_f = 75$ kHz, $G_a = -16.2$ kHz/mm, $T_a = 0.125$ ms. The FOV resulting in (B) for such set of parameters is 23.1 mm.

thus yielding a continuous version of the refocusing condition derived earlier in Eq. (5). Eq. (12) together with k's maximum absolute value $k_{max} = |G_a T_a|$, can once again be used to compute the total $FOV = |RG_a T_a / G_e^2|$. A derivation of the spatial resolution associated to the chirped excitation on the other hand, is less straightforward than its discrete counterpart. Still it is possible to invoke arguments connecting the second derivative of the overall phase Φ to the interval Δz below which it is not possible to distinguish the actual contribution of individual spins, to derive a nominal resolution given by

$$\Delta z = \sqrt{\frac{2\pi}{\left|\left(\frac{\partial^2 \Phi}{\partial z^2}\right)_{z=z_k}\right|}} \cong \sqrt{\left|\frac{2\pi R}{G_e^2}\right|} \quad \forall z. \tag{13}$$

Fig. 3 illustrates using once again 1D simulations stemming from the numerical integration of z-dependent Bloch equations, how the various arguments derived in this paragraph enable a chirped RF excitation followed by a refocusing gradient to map the spatial profile of spins within a sample. In fact on comparing these results with those calculated assuming a discrete excitation of the sample (Fig. 2), one can notice that a finer spatial resolution is born out. As further illustrated below, similar improvements are observed on using chirp excitation to carry out single-scan 2D MRI acquisitions on model phantoms.

2.3. Spatially encoded MRI using FM pulses and sinusoidal gradients

The preceding paragraphs demonstrate that non-Fourier-transform methods relying on a chirped excitation of the spins can be used to collect 1D NMR images. The sequences in Figs. 1B and C incorporate these principles along an indirect dimension, and couple it to periodic gradient reversals and blipped frequency encodings of the kind usually employed in EPI protocols in order to build a 2D imaging scheme. A well-known technical complication of all the resulting ultrafast MRI schemes is associated with their reliance on rapidly varying gradients, liable to induce strong eddy currents and neural stimulation that limit their performance and applicability [15]. Particularly challenging is the application of square-wave modulated gradients of the type proposed throughout the course of t_2 in Figs. 1B and C. Such complication can be alleviated by replacing the square-wave modulation with a sinusoidal one, an approach of widespread use in functional MRI [5,15]. Sinusoidal acquisition gradients, however, are also known to impart distortions into EPI MRI images, as they end up distributing data points in a non-uniform manner along the k-axes. Obtaining non-distorted images then requires a re-interpolation of the data into a regular equidistant grid, or the less artifact-prone but more challenging alternative of relying on non-uniform sampling dwells throughout the course of the data acquisition. As we have discussed elsewhere such distortions affect to a lesser extent spatially encoded techniques like the ones presented in this work, which do not rely on Fourier transforming k-domain data altogether [27]. Still this approach would distort the time-linearity of the decoded z coordinates implicit in Eq. (12) for the case of a constant G_a gradient; on using sinusoidal decoding gradients of the form $G_1(t) = G_a \sin(\pi t/T_a)$ for instance (Fig. 1D), the overall spatial decoding in the sequence would proceed at a rate $k = G_a T_a/\pi[1 - \cos(\pi t/T_a)]$ instead of at the usual $k = G_a \cdot t$.

The peculiar manner in which the imaging proceeds in these spatially encoded experiments actually provides a number of alternatives to reinstate the simple, desirable linearity relating the acquisition time t with the position z of spins along the sample—even when employing shaped acquisition gradients. A straightforward way to reinstate the $z \propto t$ progression while avoiding interpolation or non-linear sampling is to change the offset sweep of the chirp pulse, from a constant rate R to a time-dependent one. We derive next the frequency modulation (FM) that would then have to be employed, assuming for simplicity that a sinusoidal $G_1(t)$ gradient is used over the course of the signal acquisition. A straightforward way to derive the FM pulse that will then be required follows from the realization that even for the case of a general RF sweep, the condition in Eq. (11) that defines the coordinates z being probed by a particular wavenumber k can be recast as

$$\frac{\partial \Omega_1}{\partial z} t_1 + k = 0. \tag{14}$$

Considering then $\Omega_1(z) = G_e z$ as well as the wavenumber $k = \frac{G_a T_a}{\pi}[1 - \cos(\pi t/T_a)]$ defined by a sinusoidal gradient, translates this condition into

$$G_e \cdot t_1 = -\frac{G_a T_a}{\pi}\left[1 - \cos(\pi t/T_a)\right]. \tag{15}$$

Requesting now a linear map of z by the acquisition time t, $t = a \cdot z + b$, and recalling that in our simplified excitation model the offset O of the RF is always linearly related to the z position of the excited spins according to $z = O/G_e$, enables the use of Eq. (15) for solving the dependence that the chirped offset should exhibit as a function of t_1. The offset of the resulting FM pulse can be summarized as

$$O(t_1) = O_f + \frac{O_i - O_f}{\pi} \cdot \operatorname{arcos}\left[1 - \left|\frac{2G_e}{k_{\max}}\right| t_1\right], \tag{16a}$$

where $\{O_i, O_f\}$ are once again the initial and final offsets of the frequency sweep defining the spatial range to be explored according to $\mathrm{FOV} = (O_i - O_f)/G_e$, and $|k_{\max}| = |2G_a T_a/\pi|$ is the maximum k-value probed by the sinusoidal gradient. As discussed in connection to Eq. (7), it is often convenient to describe the offset dependence of an FM pulse as a function of the time t' elapsed since its initiation: $t' = t_1^{\max} - t_1$. Since within the present context the overall pulse duration $t_1^{\max}$ is chosen to fulfill $G_e t_1^{\max} = -k_{\max}$, Eq. (16a) can then be rewritten in an experimentally more practical form

$$O(t') = O_f + \frac{O_i - O_f}{\pi} \cdot \operatorname{arcos}\left[\frac{2t'}{t_1^{\max}} - 1\right]. \tag{16b}$$

With regard to the spatial resolution associated with this frequency modulated excitation, an analysis akin to that leading to Eq. (13) reveals a position-dependent frequency resolution given by

$$\Delta z(z) = \sqrt{\frac{2 \cdot \mathrm{FOV}}{k_{\max}\left|\sin\left(\pi \frac{z_f - z}{\mathrm{FOV}}\right)\right|}}. \tag{17}$$

Resolution is thus highest at the center of the sample and undefined at the edges of the FOV when the rate of sweep is the slowest, a drawback which can be accounted for by choosing a sweep range (and thereby an FOV value) larger than the object one is actually trying to image.

Fig. 4 validates on the basis of numerical simulations these arguments, by showing how sinusoidal acquisition gradients coupled to the suitably tuned FM pulses arising from Eq. (16a) yield a faithful spatial description of spin positions within a sample without further manipulations. Indeed $|S(k)|$ images shown in the right-hand panels of this figure are plotted directly as a function of the acquisition time t; notice that although such time variable maps the acquisition k wavenumber involved in the spatial decoding non-uniformly, the corresponding imaging features remain linear with respect to the spins' z profiles.

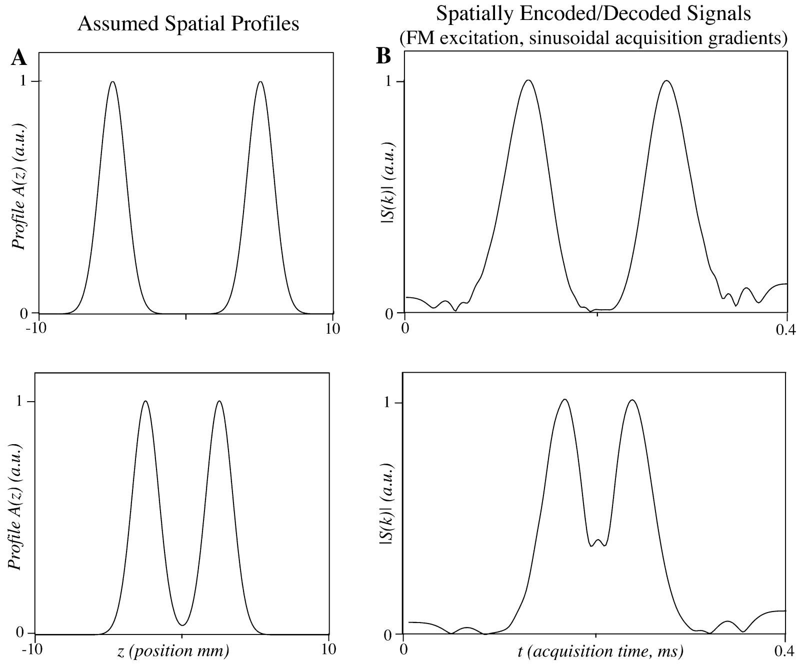

Fig. 4. Idem as in Fig. 2, but this time assuming an arcos–type frequency modulation of the RF excitation pulse and sinusoidal decoding gradients as depicted in Fig. 1D and Eq. (16a) (translated from rad s^{-1} mm^{-1} into kHz mm^{-1} units). Parameters assumed for such simulations included $G_e = 8.1$ kHz/mm, $O_i = -O_f = 100$ kHz, $T_1^{\max} = 0.4$ ms, $G_a = -12.75$ kHz/mm (maximum amplitude of the half-sine waveform), and a data acquisition time $T_a = 0.4$ ms sampled with a constant dwell of 2 μs. The FOVs resulting in the (B) panels for such parameters are 24.66 mm, while at the same time corresponding to an overall k-span of 3.25 mm^{-1}. Notice the non-uniform spatial resolution displayed by the $|S(k)|$ signals, as evidenced by the slight asymmetries in the rising and edging slopes of their humps.

2.4. Practical considerations

The previous paragraphs described a series of alternatives that could yield 2D MR images within a single scan, relying on a frequency-based encoding of the spins' spatial positions during t_1 followed by repetitive de- and re-coding processes during t_2 based on bipolar gradients. As echo planar imaging relies on technically similar detection schemes for achieving this aim, a natural question that arises is how do various practical aspects of both methods compare. In this Section we focus on two such characteristics, the signal-to-noise ratio (S/N) and the gradient strength requirements, considering on one hand spatially encoded sequences like the ones introduced in Fig. 1B or C, and on the other a comparable EPI scheme where the initial frequency-swept excitation in either of these sequences is replaced by a single $\pi/2$ pulse triggering the simultaneous evolution of all spins. Furthermore for the sake of a meaningful comparison we shall assume no customized processing (zero-filling, weighting) of the data, negligible T_2 relaxation effects, and identical noise functions characterizing both sets of time-domain data given by σ_N r.m.s. amplitudes per unit spectral bandwidth, incorporating parameters such as the coil's resistance, Q value, etc.

On pursuing a comparison between the practical characteristics of both kind of sequences one needs to address the fact that whereas in the spatially encoded schemes the k-space (or time-domain) data *is* the image, EPI schemes need to subject their $S(k)$ signals to Fourier transformation in order to obtain the z-domain image. The S/N characterizing the final image at a particular $z_k \pm \Delta z/2$ coordinate is then particularly simple to compute in the spatially encoded (s-e) case. Indeed as mentioned in connection with Eq. (6) this technique will provide time-domain signals that are directly proportional to the spatial profiles; considering then that every k-point is characterized by a $\sigma_N^{\text{s-e}}$ r.m.s. noise value S/N in this kind of experiment becomes

$$(\mathrm{S/N})_{\text{s-e}} = \frac{|S_{\text{s-e}}(k)| \cdot \Delta z_{\text{s-e}}}{\sigma_N^{\text{s-e}}} = \frac{|A(z_k)| \cdot \Delta z_{\text{s-e}}}{\sigma_N^{\text{s-e}}}, \tag{18}$$

where $\Delta z_{\text{s-e}}$ is the voxel size afforded by the spatial encoding. EPI on the other hand, will measure for every k-point signals arising from the complete sample volume:

$$S_{\text{EPI}}(k) = \int_{\text{all } z} A(z) e^{ikz}\,dz. \tag{19}$$

The image of the sample at a desired z_0 coordinate, $I_{\text{EPI}}(z_0)$, results from subjecting this k-domain function to the Fourier transform

$$I_{\text{EPI}}(z_0) = \int_{k_{\min}}^{k_{\max}} S_{\text{EPI}}(k) e^{-ikz_0}\,dk, \tag{20a}$$

which given the discrete signal sampling involved becomes a sum over the N_k digitized points

$$\begin{aligned} I_{\text{EPI}}(z_0) &= \sum_{m=-N_k/2}^{N_k/2-1} \left\lfloor \int_{\text{sample}} A(z) e^{i\cdot m\Delta k\cdot z}\,dz \right] e^{-i\cdot m\Delta k\cdot Z_0} \\ &\approx N_k \cdot \Delta z_{\text{EPI}} \cdot A(z_0), \end{aligned} \tag{20b}$$

Δz_{EPI} is now the voxel resolution of the method, given by $(\Delta k \cdot N_k)^{-1}$. As for the noise characterizing such profile, this can be found by replacing the $S_{\text{EPI}}(k)$ signal in Eqs. (20a) and (20b) with the random noise introduced in the preceding paragraph. When implementing on this random function the sum associated to the discrete Fourier transform, the resulting noise amplitude increases as the root of the number of added points

$$N(z_0) = \sqrt{N_k} \cdot \sigma_N^{\text{EPI}}. \tag{21}$$

The overall S/N characterizing the EPI-derived images can thus be summarized as

$$(\mathrm{S/N})_{\text{EPI}} = \left| \frac{I_{\text{EPI}}(z_0)}{N(z_0)} \right| = \sqrt{N_k} \cdot \Delta z_{\text{EPI}} \cdot \frac{|A(z_0)|}{\sigma_N^{\text{EPI}}}. \tag{22}$$

A comparison between Eqs. (18) and (22) suggests that for identical Δz spatial resolutions, S/N in traditional EPI MRI experiments will be higher than in our new spatially encoded methods by a factor $\sqrt{N_k}$. This, however, would ignore the fact that whereas in conventional Fourier schemes the reception system needs to accommodate the complete frequency distribution spanned by the FOV, images arise in the spatial encoding scheme in a voxel-by-voxel fashion. Receiver bandwidths thus need to extend over a $G_a \cdot N_k \Delta z$ range in the former case, while spanning only $G_a \cdot \Delta z$ for the latter. The ratio between the bandwidth-controlled noise factors in the two schemes thus becomes $(\sigma_N^{\text{EPI}}/\sigma_N^{\text{s-e}}) = \sqrt{N_k}$, leading then to identical S/N for both kinds of acquisitions. Such coincidence, however, does not mean that all practical requirements for the EPI and the spatial encoding approaches end up being identical. In fact following the various definitions and arguments given above, it can also be shown that requesting identical FOV's and Δz's for both kinds of acquisition schemes leads to the condition $k_{\max}^{\text{s-e}} = \sqrt{N_k} k_{\max}^{\text{EPI}}$. In other words, the spatial encoding approach requires either longer sequences or more intense gradients than currently available methods for obtaining images of identical characteristics. This difference can be rationalized from the fact that whereas in EPI experiments every Δz voxel contributes to the k-space signal throughout the course of all N_k detected points, contributions from independent voxels in the spatial-encoding experiment are unraveled in a k-sequential point-wise manner.

3. Results and discussion

The theoretical arguments presented in the preceding sections were tested with a series of single-scan 2D MRI

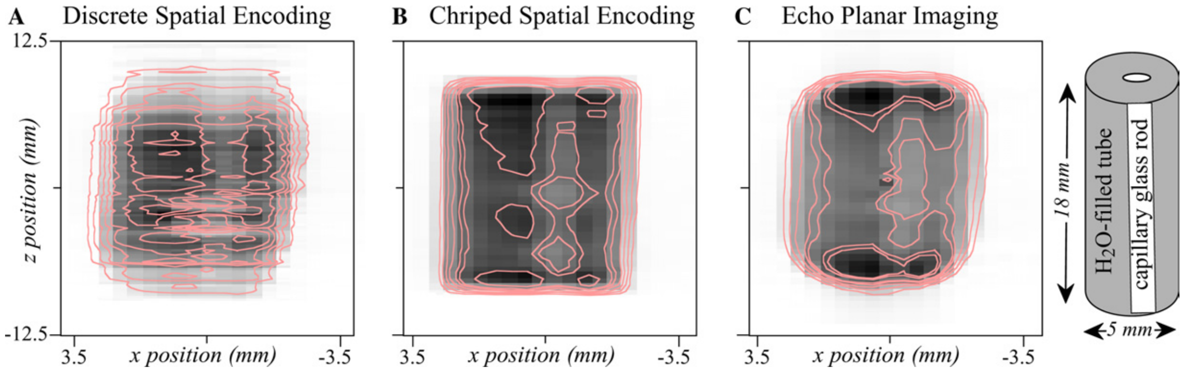

Fig. 5. Results obtained with different single-scan 2D imaging protocols when applied on the phantom illustrated on the right (illustrated for ease of comparison as superimposed contour/grayscale plots). (A) Profile obtained upon using the discrete spatial encoding sequence in Fig. 1B, with G_1 corresponding to a gradient applied along the z axis and G_2 to a gradient along the x direction. Experimental conditions were $G_e = 9.2$ kHz/mm, $N_1 = 16$, 0.1-ms-long square excitation pulses spaced $\Delta O = 10$ kHz apart, $|G_a| = 13.5$ kHz/mm, $T_a = 0.98$ ms (plus 20 μs gradient switching times), $N_2 = 20$, and the x-encoding done by 40-μs-long half-sine gradient pulses with 2.4 kHz/mm maximum strength. Notice that as was the case for the simulation in Fig. 2, this image evidences the discrete nature of the spatial encoding that took place along the z axis. (B) Idem as in panel (A) but using the chirped spatial encoding version depicted in Fig. 1B. Spatially encoding/decoding parameters here included $G_e = 8.1$ kHz/mm, $t_1^{max} = 0.28$ ms, $O_i = -O_f = 75$ kHz, $|G_a| = 16.2$ kHz/mm, $T_a = 0.152$ ms (plus 16 μs gradient switching times), and an x spatial encoding done as in (A). (C) EPI acquisition based on a pulse sequences analogous to that illustrated in Fig. 1B, but with the initial spatial-dependent encoding replaced by a single hard $\pi/2$ excitation pulse acting simultaneously on all spins in the sample. Acquisition parameters (using the notation given in Fig. 1B) included $|G_a| = 9.2$ kHz/mm, $T_a = 0.152$ ms (plus 16 μs gradient switching times), and an x spatial encoding as in (A). Sampling dwell times were in all cases 4 μs.

experiments on a Bruker Avance 800 MHz NMR spectrometer equipped with an inverse probehead and a triple-axis gradient.[3] Assayed in these tests were the discrete and chirped pulse sequences introduced in Figs. 1B and C, with the indirect-domain spatial encoding executed with the aid of a longitudinal z gradient and the direct t_2 frequency encoding with a transverse x one. For the sake of comparison, 2D blipped EPI single-scan images were also recorded. A variety of Matlab 6.5 software programs (The MathWorks) were written for the sake of reading, processing and simulating all these data.

Two kinds of phantoms were prepared for the tests, both on the basis of conventional 5 mm NMR tubes. One of phantoms incorporated a transverse heterogeneity in the form of an empty longitudinal capillary centered in an NMR tube filled with a D_2O/H_2O solution. The second phantom was made up by three contiguous layers of water-saturated polyacrilamide gel; here the central layer was doped with $CoCl_2$ and failed to appear in T_2-weighted imaging experiments, thus providing a longitudinal heterogeneity. Figs. 5 and 6 illustrate results obtained when the various single-scan 2D MRI pulse sequences were applied to these two phantoms. As can be appreciated the main features of the phantoms are revealed by all the methods, even if it is clear that the chirped RF and EPI protocols provide the highest quality images. It is illustrative to compare the relative sensitivity of these two experiments. According to the various acquisition parameters employed (sweep rate R, excitation and acquisition gradients G_e, G_a, dwell time Δ, filter bandwidth t) Eqs. (18) and (22) predict that S/N in the EPI image shown in Fig. 5C should be 1.8 times higher than in the spatially encoded counterpart shown in Fig. 5B; the numerically measured ratio between the relative sensitivities of both experimental data, as judged by extracting different slices from the corresponding image sets, came closer to 2.5. A similar theoretical S/N estimate for the images reported in Fig. 6 predicts that EPI's sensitivity should be 1.5 times higher than that of its spatially encoded counterpart, while a numerical analysis of the experimental cross sections revealed this factor to be 1.4.

The purpose of the present study was to introduce a new member to the family of methods available for fast 2D MR imaging. So far, this important goal could be achieved by following basically two kinds of approaches. One of these involved executing a conventional k-space encoding utilizing low excitation angles and thereby supporting a very rapid repetition [28]; the other involved an EPI-derived sampling of the complete k-space data matrix based on continuous trains of modulated spin echoes [11]. The new approach that is hereby described is comparable to EPI and its variants in that it can provide multidimensional MRI images within a single transient, but differs from all approaches hitherto proposed in that it does not rely on the acquisition of a k-space data matrix and on its subsequent Fourier transformation, but rather on a spatial encoding of the indirect-domain evolution. Although in terms of its

---

[3] The high field and sophisticated multi-resonance equipment used in these tests was the result of circumstantial availability, rather than stemming from demands of the experiments themselves.

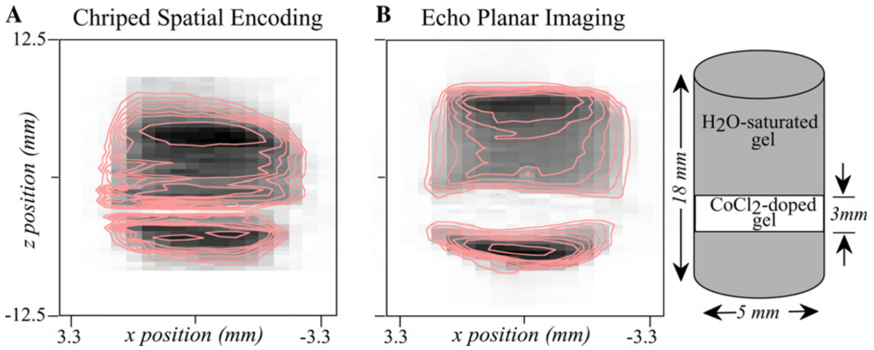

Fig. 6. Idem as in Fig. 5, but this time with experiments implemented on the longitudinally inhomogeneous phantom schematized on the right. (A) Contour plot obtained upon employing the chirped spatial encoding version depicted in Fig. 1C with parameters $G_e = 7.5$ kHz/mm, $t_1^{max} = 0.39$ ms, $O_i = -O_f = 75$ kHz, $|G_a| = 20$ kHz/mm, $T_a = 0.152$ ms (plus 16 μs gradient switching times). (B) Single-scan EPI image collected using the same parameters as in Fig. 5C. The x spatial encoding and the rates of data digitization employed for both experiments were also as described in Fig. 5.

practical demands it is predicted by theory that this new ultrafast 2D MRI acquisition mode may not perform as efficiently as other existing rapid imaging techniques, it is already clear that the excitation and acquisition modalities described throughout the present work can play important roles in various single-scan 2D spectroscopy applications [29]. It is also worth noting that spatial encoding offers promising opportunities to compensate a variety of field and RF inhomogeneities [30], a feature that can be easily incorporated into the MRI protocol hereby described. A description of this new compensation protocol will be given in an upcoming publication.

Acknowledgments

We are grateful to Ms. Dina Aronzon (K. Kupcinet 2003 Summer School, Weizmann Institute) for assistance in preparing the polyacrilamide gel phantoms. This work was supported by the Philip M. Kluztnick Fund for Research, by the Minerva Foundation (Munich, FRG), as well as by a grant from the Henry Gutwirth Fund for the Promotion of Research.

Appendix A. Derivation of optimal excitation conditions for a linearly swept RF chirp pulse

From the standpoint of both MRI and NMR ultrafast acquisitions, the use of a continuous frequency-swept RF irradiation offers a promising route to an optimal spatial encoding of the interactions. The purpose of such RF pulse should be to maximize during the course of its sweep, the amount of observable magnetization that is excited throughout the sample starting from an initial $M_0 = I_z$ reduced density matrix state. For the simplest case of a linearly swept chirp pulse the parameter defining a pulse's performance is $\alpha = (\Omega_{RF})^2/R$, depending on the nutation rate Ω_{RF} imparted by the RF and on the rate R at which frequency offsets are swept. Fig. 7 illustrates this feature by showing how the average tilt angle θ imparted by a chirped excitation pulse on an inhomogeneously broadened sample, varies as a function of the inverse sweep rate from $\theta \approx 0$ when the sweep is fast compared to Ω_{RF} ($\alpha \ll 1$: sudden passage), to $\theta \approx \pi$ when the sweep rate is very slow ($\alpha \gg 1$: adiabatic inversion). The conditions assumed throughout Sections 2 and 3 of this study actually differ from any one of these two extremes, as there it was assumed that the chirped pulse applies a nearly complete $\theta = \pi/2$ nutation on the spins. For the sake of completion we present in this Appendix how to achieve an optimized spin excitation under such intermediate passage conditions.

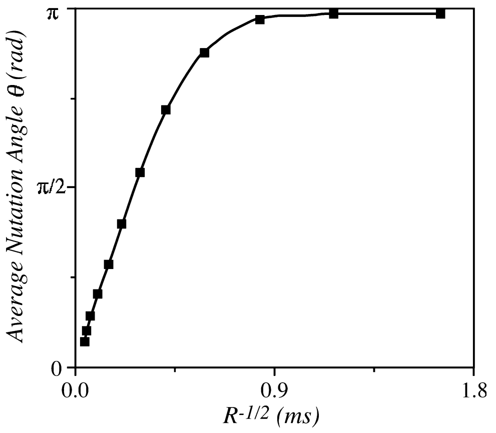

Fig. 7. Average nutation angle θ excited throughout the sample by a chirped RF pulse defined by a sweep rate $R = \left|\frac{\partial \Omega}{\partial t}\right|$, plotted as a function of $R^{-1/2}$. The square dots indicate results from numerical calculations where an $\Omega_{RF} = 1$ kHz nutation field was swept for different lengths of time from +75 kHz above to −75 kHz below resonance, while a constant $G_e = 8.1$ kHz/mm gradient was applied on an 18 mm long sample. These calculations involved partitioning the sample into a large number of individual z coordinates, and then propagating within a common rotating frame the time evolution of spins positioned at such differing coordinates.

Several treatments on how to propagate the spin evolution under the effect of a Hamiltonian incorporating both a longitudinal gradient and a linearly swept RF pulse have been presented in the literature [31]. These treatments usually pertain adiabatic inversions rather than transverse excitations, yet the two processes share a common scenario and thus we found it convenient to incorporate their existing conventions in this account. According to these adiabatic sweep guidelines it is convenient to calculate the evolution of spins' by implementing a series of transformations whereby the initial rotating-frame Hamiltonian[4]

$$\begin{aligned} H_{\text{rot-frame}}(t) &= \Omega_1 I_z + \Omega_{\text{RF}}\left\{\cos\left[\int_0^t O(t')\,\mathrm{d}t'\right] I_x + \sin\left[\int_0^t O(t')\,\mathrm{d}t'\right] I_y\right\} \\ &= G_z z I_z + \Omega_{\text{RF}}\left\{\cos\left\{\int_0^t [O_{\text{i}} - R\cdot t']\,\mathrm{d}t'\right\} I_x + \sin\left\{\int_0^t [O_{\text{i}} - R\cdot t']\,\mathrm{d}t'\right\} I_y\right\} \end{aligned} \tag{A.1}$$

is first transformed into a FM-frame to yield

$$H_{\text{FM}}(t) = [\Omega_1 - O(t)]I_z + \Omega_{\text{RF}} I_x, \tag{A.2}$$

and then into an effective-field frame driven at a rate $\Omega_{\text{eff}}(t) = \sqrt{[\Omega_1 - O(t)]^2 + \Omega_{\text{RF}}^2}$ to yield

$$H_{\text{eff}}(t) = \Omega_{\text{eff}}(t) I_z + \frac{R\cdot\Omega_{\text{RF}}}{[\Omega_{\text{eff}}(t)]^2} I_y. \tag{A.3}$$

It is been shown by Haase et al. that the norm of this effective Hamiltonian can be further reduced by rotating it at a rate $\Omega_{\text{eff}}(t)$ about the I_z axis [32], leading to

$$\tilde{H}_{\text{eff}}(t) = \frac{R\cdot\Omega_{\text{RF}}}{[\Omega_{\text{eff}}(t)]^2}\{I_y \cos[\sigma(t)] - I_x \sin[\sigma(t)]\}, \tag{A.4}$$

where $\sigma(t) = \int \Omega_{\text{eff}}(t')\,\mathrm{d}t'$. The evolution operators driving these three transformations are in turn given by

$$U_{\text{FM}}(t) = \exp\left[\mathrm{i}\cdot\left(\int_0^t O(t')\,\mathrm{d}t'\right)\cdot I_z\right], \tag{A.5}$$

$$U_{\text{eff}}(t) = \exp\left\{-\mathrm{i}\cdot\arctan\left[\frac{\Omega_{\text{RF}}}{\Omega_1 - O(t)}\right]\cdot I_y\right\} \tag{A.6}$$

and

$$U_z(t) = \exp\left[\mathrm{i}\cdot\left(\int_0^t \Omega_{\text{eff}}(t')\,\mathrm{d}t'\right)\cdot I_z\right], \tag{A.7}$$

respectively.

In spite of all these transformations the Hamiltonian in Eq. (A.4) is still non-self-commuting and time-dependent; most of its fast-oscillating behavior, however, has been accounted for by the various frame transformations. Its effects on spins evolving in its accelerated reference frame can therefore be approximated to first order as

$$\tilde{U}(t) = \exp\left\{-\mathrm{i}\cdot\int_t \tilde{H}_{\text{eff}}(t')\,\mathrm{d}t'\right\}, \tag{A.8}$$

where the time integration runs through the course of the frequency sweep. Applying these various interaction transformations to an initial density matrix state $\rho_0 = I_z$, and extracting the coefficients multiplying the I_x, I_y terms in the resulting $\rho(t)$ to calculate the transverse magnetization that has been excited by the action of the frequency chirp, leads then to

$$|M_\perp(t)| = \sin\left\{R\Omega_{\text{RF}}\int_{t_1}\frac{\cos[\sigma(t')]}{[\Omega_{\text{eff}}\cdot(t')]^2}\,\mathrm{d}t'\right\}. \tag{A.9}$$

Finally, we assume that the effects of the frequency swept are only felt by spins when the pulse is approximately on-resonance; that is in the $O \approx G\cdot z$ neighborhood, where $\Omega_{\text{eff}} \approx \Omega_{\text{RF}}$. This enables an analytic calculation of the time integral in Eq. (A.9) and predicts an excited transverse magnetization

$$|M_\perp(t)| = \sin\left\{\frac{R}{\Omega_{\text{RF}}^2}\sin\left(\frac{\Omega_{\text{RF}}^2}{R}\right)\right\}. \tag{A.10}$$

An appealing aspect of this result is that in accordance with the arguments put forward at the beginning of this Appendix, it predicts an efficiency of the chirped excitation that is dependent on the adiabaticity parameter $\alpha = |(\Omega_{\text{RF}})^2/R|$ rather than on the independent values

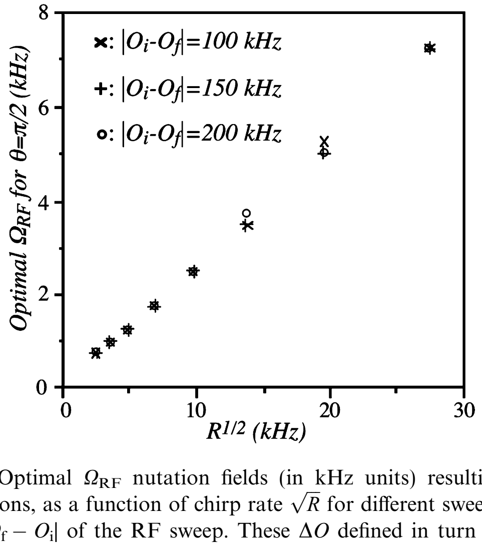

Fig. 8. Optimal Ω_{RF} nutation fields (in kHz units) resulting from calculations, as a function of chirp rate $\sqrt{R}$ for different sweep ranges $\Delta O = |O_{\text{f}} - O_{\text{i}}|$ of the RF sweep. These ΔO defined in turn an FOV [approx] 18 mm, as related by excitation gradients $G_{\text{e}} = 5.4$, 8.1, and 10.8 kHz/mm for $\Delta O = 100$, 150, and 200 kHz respectively. Simulations were carried out by propagating the Bloch equations (cf. Fig. 7) and the optimal Ω_{RF} was in each case defined as corresponding to the RF that maximized the absolute value of the transverse magnetizations excited throughout the sample.

---

[4] t here is the time elapsed since beginning the chirped excitation, connected to the evolution t_1 mentioned elsewhere in the manuscript as $t = t_1^{\max} - t_1$.

of R or Ω_{RF}. A graphic analysis following from setting the derivative of Eq. (A.10) to zero predicts that the maximum transverse magnetization will be excited when the adiabaticity parameter becomes $\alpha \approx 0.16$.

In an effort to verify the validity of this prediction extensive sets of numerical simulations were carried out, focused on finding which nutation fields would maximize the overall magnetizations excited in the presence of a constant gradient. Fig. 8 summarizes some of these numerical investigations by plotting, for a variety of sweep ranges and of gradient strengths, the Ω_{RF} value found to maximize the excited transverse magnetization for different sweep rates R. In all cases a nearly perfect linearity between to optimum Ω_{RF} and $\sqrt{R}$ is found regardless of any other conditions; the maximum magnetization is usually excited when the chirped RF field fulfills

$$(\Omega_{\mathrm{RF}})_{\mathrm{opt}} \approx 0.26\sqrt{R}. \tag{A.11}$$

This value is ca. 35% smaller than the prediction above, not an unreasonable deviation in view of the approximations involved in the theoretical analysis.

References

[1] D.M. Grant, R.K. Harris, Encyclopedia of NMR, Wiley, Chichester, 1996.

[2] J. Jeener, Lecture presented at Ampere International Summer School II, Basko Polje, Yugoslavia, September, 1971, in: M. Goldman, M. Porneuf (Eds.), Les editions de physique, Lecture notes published in NMR and more in honor of Anatole Abragam, Les Ulis, France, 1994.

[3] W.P. Aue, E. Bartholdi, R.R. Ernst, Two dimensional spectroscopy. Application to nuclear magnetic resonance, J. Chem. Phys. 64 (1976) 2229–2246.

[4] P. Mansfield, P.G. Morris, NMR Imaging in Biomedicine, Academic, New York, 1982.

[5] M.A. Brown, R. Semelka, MRI: Basic Principles and Applications, Wiley-Liss, New York, 1999.

[6] A. Kumar, R.R. Ernst, NMR Fourier zeugmatography, J. Magn. Reson. 18 (1975) 69–83.

[7] R.R. Ernst, G. Bodenhausen, A. Wokaun, Principles of Nuclear Magnetic Resonance in One and Two Dimensions, Clarendon, Oxford, 1987.

[8] D.B. Twieg, The *k*-trajectory formulation of the NMR imaging process with applications in analysis and synthesis of imaging methods, Med. Phys. 10 (1983) 610–621.

[9] A. Macovski, Volumteric NMR imaging with time-varying gradients, Magn. Reson. Med. 2 (1985) 29–40.

[10] D.Q. Chen, R.B. Marr, P.C. Lauterbur, Reconstruction from NMR data acquired with imaging gradients having arbitrary time dependence, IEEE Trans. Med. Imaging 5 (1986) 162–164.

[11] P. Mansfield, Multi-planar image formation using NMR spin echoes, J. Phys C: Solid State Phys. 10 (1977) 55–58.

[12] M.K. Stehling, R. Turner, P. Mansfield, Echo-planar imaging: magnetic resonance in a fraction of a second, Science 254 (1991) 43–50.

[13] I.J. Lowe, R.B. Wysong, DANTE ultrafast imaging sequence (DUFIS), J. Magn. Reson. B 101 (1993) 106–109.

[14] F. Hennel, Multiple-shot echo planar imaging, Concepts Magn. Reson. 9 (1997) 43–58.

[15] F. Schmidt, M.K. Stehling, R. Turner, Echo Planar Imaging: Theory, Technique and Application, Springer, Berlin, 1998.

[16] A. Bax, A.F. Mehlkoff, J. Smidt, A fast method for obtaining 2D *J*-resolved absorption spectra, J. Magn. Reson. 40 (1980) 213–219.

[17] P. Blumler, J. Jansen, B. Blümich, Two-dimensional one-pulse rotational echo spectra, Solid State NMR 3 (1994) 237–240.

[18] L. Frydman, J. Peng, Non-Cartesian sampling schemes and the acquisition of 2D NMR correlation spectra from single-scan experiments, Chem. Phys. Lett. 220 (1994) 371–377.

[19] L. Frydman, T. Scherf, A. Lupulescu, The acquisition of multidimensional NMR spectra within a single scan, Proc. Natl. Acad. Sci. USA 99 (2002) 15858–15862.

[20] L. Frydman, T. Scherf, A. Lupulescu, Principles and features of single-scan two-dimensional NMR spectroscopy, J. Am. Chem. Soc. 125 (2003) 9204–9217.

[21] Y. Shrot, L. Frydman, Single-scan NMR spectroscopy at arbitrary dimensions, J. Am. Chem. Soc. 125 (2003) 11385–11396.

[22] B. Shapira, L. Frydman, Arrayed acquisition of 2D exchange NMR spectra within a single experiment, J. Magn. Reson. 165 (2003) 320–324.

[23] B. Shapira, A. Lupulescu, Y. Shrot, L. Frydman, Line shape considerations in ultrafast2D NMR, J. Magn. Reson. 166 (2004) 152–164.

[24] Y. Shrot, L. Frydman, Spatially resolved multidimensional NMR spectroscopy within a single scan, J. Magn. Reson. 167 (2004) 42–48.

[25] A. Abragam, Principles of Nuclear Magnetism, Oxford University Press, Oxford, 1961 (Chapter 2).

[26] P. Pelupessy, Adiabatic single-scan 2D NMR spectroscopy, J. Am. Chem. Soc. 125 (2003) 12345–12350.

[27] N. Sela, H. Degani, L. Frydman, Ultrafast 2D NMR using sinusoidal gradients: principles and ex-vivo brain investigations, Magn. Reson. Med. 52 (2004) 893–897.

[28] J. Frahm, A. Haase, D. Matthaei, Rapid NMR imaging of dynamic processes using the FLASH technique, Magn. Reson. Med. 3 (1986) 321–327.

[29] Y. Shrot, B. Shapira, L. Frydman, Ultrafast 2D NMR spectroscopy using a continuous spatial encoding of the spin interactions, J. Magn. Reson. 171 (2004) 162–169.

[30] B. Shapira, L. Frydman, Spatial encoding and the acquisition of high resolution NMR spectra in inhomogeneous fields, J. Am. Chem. Soc. 126 (2004) 7184–7185.

[31] See for instance M. Garwood, L. DelaBarre, The return of the frequency sweep: designing adiabatic pulses for contemporary NMR, J. Magn. Reson. 153 (2001) 155–177 (and references therein).

[32] J. Haase, M.S. Conradi, C.P. Grey, A.J. Vega, Population transfers for NMR of quadrupolar spins in solids, J. Magn. Reson. A109 (1994) 90–95.